Electrochimica Acta 448 (2023) 142155

Contents lists available at ScienceDirect

Electrochimica Acta

journal homepage: www.journals.elsevier.com/electrochimica-acta

On the rising extra storage capacity of ultra-small Fe_3O_4 particles functionalized with HCS and their potential as high-performance anode material for electrochemical energy storage

Lennart Singer [a,*], Wojciech Kukułka [b], Elisa Thauer [a], Nico Gräßler [c], Andika Asyuda [d], Michael Zharnikov [d], Ewa Mijowska [b], Rüdiger Klingeler [a,*]

[a] Kirchhoff Institute for Physics, Heidelberg University, Heidelberg, 69120, Germany
[b] Faculty of Chemical Technology and Engineering, West Pomeranian University of Technology, Szczecin, 71-065, Poland
[c] Leibniz Institute for Solid State and Materials Research Dresden e.V., Dresden, 01069, Germany
[d] Applied Physical Chemistry, Heidelberg University, Heidelberg, 69120, Germany

ARTICLE INFO

Keywords:
Fe_3O_4
Carbon composite
Extra storage capacity
Lithium-ion battery

ABSTRACT

We report a nanocomposite material exhibiting ultra-small Fe_3O_4 nanoparticles uniformly decorated on hollow carbon spheres (Fe_3O_4@HCS). The unique hierarchically-structured material displays excellent electrochemical cycling performance that exceeds the theoretical bulk capacity of Fe_3O_4 when used as an anode in lithium-ion batteries. In particular, it features increasing reversible capacity upon cycling yielding 1050 mAh g^{-1}at 0.1 A g^{-1} in cycle 250. Comprehensive scanning and transmission electron microscopy images combined with detailed electrochemical analysis demonstrate that the outstanding electrochemical performance can be traced back to the formation and decomposition of a capacitative surface layer during dis/charging.

1. Introduction

Over the past three decades, due to their high energy density, high Coulombic efficiency, and long cycle life, rechargeable lithium-ion batteries (LIBs) have been widely used in portable electronic devices, stationary energy storage devices, and electric vehicles. However, there is still a gap between existing batteries as well as their active electrode materials and, the enormous demand for batteries with ever higher energy density, cycle stability and environmental compatibility. Therefore, the development of alternative battery materials is imperative. Transition metal oxides (TMOs), with their attractive theoretical (bulk) capacities due to the multiple-electron transfer conversion reaction taking place with Li^+ ions are considered a promising alternative anode material for LIBs [1–8]. Among them, based on its low cost, environmentally friendly nature, and high theoretical capacity of 926 $mAhg^{-1}$, Fe_3O_4 is one of the most promising anode materials for the next-generation of LIBs [1,9–11]. However, large volume changes of Fe_3O_4 anodes during cycling, leading to particle cracking, electrode pulverization and premature electrode collapse, prevent full exploitation of Fe_3O_4 as a LIB anode material [12]. To address these issues, several strategies have been developed to improve the structural integrity of Fe_3O_4-based anode materials, like the fabrication of Fe_3O_4-carbon composites and particle size reduction to the nanometer-scale [13]. Particularly, downsizing of Fe_3O_4 particles into the few nanometer regime has been found to result in further positive effects such as the possibility to even exceed the proposed theoretical bulk capacity [10,14,15]. For the observed extra capacity, two different scenarios are discussed in the literature: (1) surface side reactions including the SEI [1,16] and/or (2) storage of spin polarized electrons at the surface of the formed iron metal particles [17] described by interfacial charge storage theory [18–20]. In both scenarios, the amount of additional stored charges strongly depends on the size and surface area of the electrochemically formed iron particles. The smaller the formed iron particles, the greater their combined surface area and surface to volume ratio, leading to more possible reaction sites. The size of the electrochemically formed iron particles in turn strongly depends on the size of the pristine Fe_3O_4 particles in the material [10,14,17]. Beyond the amount of additional capacity of nanoscaled Fe_3O_4, most of the materials do not reach maximum capacity directly, they instead exhibit an increasing capacity during cycling. The phenomenon of the increasing capacity during cycling is even less understood and discussed in literature as the origin behind the extra capacity of Fe_3O_4. One powerful way to investigate both, the origin and the rise of the extra capacity is electrochemical impedance spectroscopy (EIS). EIS allows to study complex electrochemical processes and kinetics with the

* Corresponding authors.
E-mail addresses: lennart.singer@kip.uni-heidelberg.de (L. Singer), klingeler@kip.uni-heidelberg.de (R. Klingeler).

https://doi.org/10.1016/j.electacta.2023.142155
Received 15 December 2022; Received in revised form 23 February 2023; Accepted 27 February 2023
Available online 2 March 2023

ability to deconvolute them into elementary processes according to the difference in the specific relaxation time constants [21–24]. This can particularly be used to invisible interfaces and surface layer, like the SEI and the double-layers [21–24]. Following the theories concerning the extra capacity EIS promises to be an ideal tool to get a deeper insight into the phenomenon of extra capacity and the rise of it. We report the hybrid material Fe_3O_4@HCS exhibiting exceptionally small Fe_3O_4 particles uniformly distributed on hollow carbon spheres. The presented Fe_3O_4@HCS impress not only with a compelling electrochemical performance of 1050 mAh g^{-1} at 0.1 A g^{-1} in cycle 250, it also displays an distinctive extra capacity with a constant increase during cycling. Our detailed electrochemical studies on Fe_3O_4@HCS combined with deep in situ electrochemical impedance spectroscopy measurements which are completed wit ex situ SEM und TEM images enabled to clarify the picture behind the extra capacity of Fe_3O_4 and its rise. Our results demonstrate, that the reversibly, growing extra capacity, reaching values well beyond the theoretical capacity can be traced back to an gradual formation and decomposition of a capacitive surface layer.

2. Experimental section

Synthesis of SiO_2–NH_2 template

To begin, a template for the growth of the final structure was prepared. For that, 6 ml of tetraethoxysilane (TEOS) was added drop wise, to a ethanol (200 ml), $NH_3 \cdot H_2O$ (10 ml) mixture and stirred at room temperature for 24 h. In order to attach NH_2 groups to the silica, additional functionalization with (3-Aminopropyl)triethoxysilane (APTES) was performed. This was done by adding 0.6 ml of APTES to the prepared mixture and stirred for the next 4 h. Finally, the obtained sample was centrifuged and the sediment was dried at 60 °C overnight.

Synthesis of carbon spheres from glucose (HCS)

In order to cover the SiO_2-NH_2 with a glucose layer, 0.6 g of the SiO_2-NH_2 prepared in the previous step and 0.6 g of glucose were added to 100 ml of water and sonicated for 30 min. Coating was then done in an Teflon-lined autoclave at 180 °C for 12 h. After, the glucose-coated silica was placed in a tube furnace, carbonization was carried out at 800 °C for 2 h under nitrogen atmosphere. Finally, the silica was removed with HF to obtain hollow carbon spheres based on glucose.

Synthesis of carbon spheres functionalized with iron oxide nanoparticles (Fe_3O_4@HCS)

Functionalization of hollow carbon spheres with iron oxide nanoparticles was performed by mixing 100 mg of HCS and 50 mg of iron(III) acetylacetonate in 30 ml triethylenglycol followed by sonication for 30 min. The mixture was then heated under reflux and nitrogen atmosphere to 278 °C at a heating rate of 3 °C/min. After cooling the mixture to room temperature, the product was precipitated with ethanol, washed and dried at 60 °C overnight.

Characterization

X-ray diffraction (XRD) patterns were acquired on a Bruker AXS D8 Advance Eco using Cu Kα radiation with a step size of $2\theta = 0.02°$. The carbon content was determined by CHN analysis on a Elementar Vario MICRO Cube. The morphology of the powder was studied using a JEOL JSM-7610F scanning electron microscope (SEM) and a transmission electron microscope with EDS attachment (TEM, Tecnai F30). Raman spectra were measured using a Via Raman Microscope (Renishaw) with an excitation wavelength of 785 nm. X-ray photoelectron (XP) spectra were measured with a MAX200 (Leybold-Heraeus) spectrometer equipped with a non-monochromatized Mg Kα X-ray source (200 W) and a hemispherical analyzer. The powder materials were pressed into clean indium foil and thinned by a brush to suppress charging effects, following established methodology [25]. Magnetic measurements were performed on Fe_3O_4@HCS powder samples using an MPMS3 magnetometer (Quantum Design). Magnetization was measured by varying the temperature between 2 and 300 K using zero-field-cooled (ZFC) and field-cooled (FC) protocols at 0.05 T. Isothermal magnetization was studied at 2 and 200 K in magnetic fields up to ±7 T.

Electrochemical measurements

Electrochemical measurements were performed on a VMP3 potentiostat (BioLogic) at 25 °C. Working electrodes were prepared by mixing the active material 80%wt, carbon black (TIMCAL SUPER C65) 10%wt, and polyvinylidene fluoride (PVDF) 10%wt in N-methyl-2-pyrrolidinone (NMP). The mixture was then stirred for 24 h before spreading the resulting slurry on (Ø=10mm, thickness=0.25 mm, weight=53.8 mg) copper mesh current collectors (see [26]). The as-prepared electrodes were dried in a vacuum oven (80 °C, 10 mbar) overnight, then pressed and dried again. The active material mass loading of the prepared electrodes ranged between 0.9 and 1.7 mg cm^{-2}. Glass fiber (Whatman GF/D, 675 µm thickness) was used as the separator and pure lithium metal foil (Aldrich) as the counter electrode. As electrolyte 120 µl of 1 M $LiPF_6$ in a mixture of ethylene carbonate and dimethyl carbonate (1:1 by weight) was used. CR 2032 coin cells were used for cyclic voltammetry and galvanostatic cycle measurements with potential limitation (GCPL). For potentiostatic electrochemical impedance measurements (PEIS), a 3-electrode PAT-Cell from EL-CELL was used, with a ring-shaped lithium metal reference electrode close to the working electrode. Cell assembly was performed in an Ar-filled glovebox with controlled humidity and oxygen concentration. Cyclic voltammetry was performed at a scan rate of 0.1 mVs^{-1}, GCPL at specific currents, each in the voltage range of 0.01–3.0 V vs. Li/Li^+. For the normalization of the specific capacity, the mass of all electrochemically active materials is taken into account, i.e. carbon black plus Fe_3O_4@HCS. For the PEIS measurements, the small disturbance of 10 mV in the frequency range from 200 kHz to 1 mHz was selected. To ensure time invariance of the measurement as well as a steady state, a 16 h OVC (open circuit voltage) was performed before each PEIS measurement, and a second control PEIS measurement was performed directly afterwards. For monitoring the micro-structural changes of Fe_3O_4@HCS during cycling, ex-situ SEM, TEM images were acquired using a JEOL JSM-7610F scanning electron microscope and a Tecnai F30 TEM, respectively. The cycled electrodes were disassembled in an argon glove box, washed with ethylene carbonate, and then dried overnight.

3. Results and discussion

3.1. Structure, morphology, and composition of Fe_3O_4@HCS

Fig. 1 shows X-ray diffractograms of the synthesized materials, i.e., Fe_3O_4@HCS and pure HCS. For HCS, a broad diffraction peak is observed around $2\theta \approx 23.5°$, which is characteristic of graphite and can be attributed to the (002) planes of graphitic carbon. This broad shoulder is also seen in the XRD pattern of Fe_3O_4@HCS, where additional Bragg reflections are observed, signaling a cubic spinel iron oxide structure, namely Fe_3O_4 (magnetite) or $\gamma - Fe_2O_3$ (maghemite). Since the XRD patterns of magnetite and maghemite are very similar, the XRD data alone do not distinguish these structures [29,30]. We also note that the respective Bragg peaks are rather broad and of low-intensity which may be attributed to small crystal size and/or low crystallinity of Fe_xO_y-particles present in the composite [31]. The average primary crystallite size of the as-synthesized samples was estimated using Scherrer's equation [32],

$$D_{hkl} = \frac{K\lambda}{\Delta(2\theta_{hkl})\cos\theta_{hkl}} \quad (1)$$

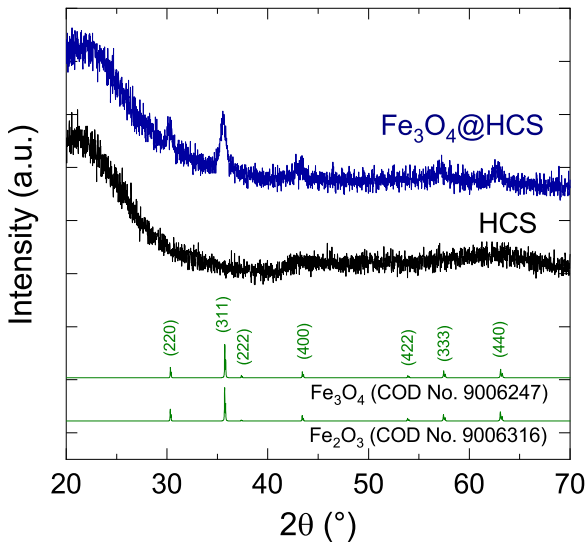

Fig. 1. XRD patterns of HCS and Fe_3O_4@HCS as well as indexed reference patterns for $\gamma - Fe_2O_3$ COD No. 9006316 [27] and Fe_3O_4 COD No. 9006247 [28].

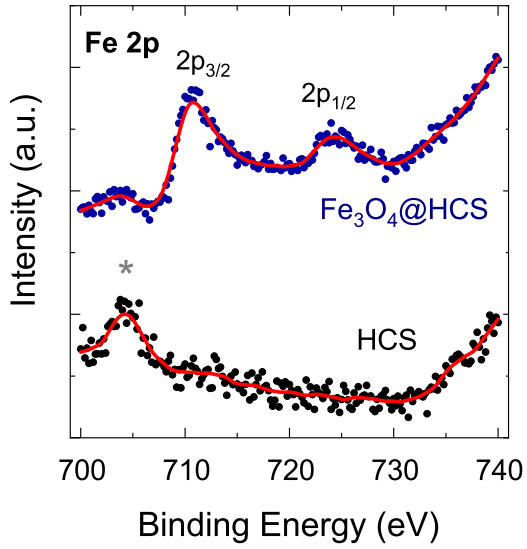

Fig. 2. Fe2*p* XP spectra of Fe_3O_4@HCS and HCS. The red solid lines show a binning of the data points. The peak marked by the asterisks originates from the used In substrate (In $3p_{1/2}$).

where D is the average crystal grain size based on the respective reflective crystal face direction (hkl), K a shape factor that can be approximated to 0.9, λ is the wavelength of the applied Cu K_α radiation, $\Delta(2\theta_{hkl})$ the full width at the half maximum of the diffraction peak, and θ_{hkl} the Bragg angle. The analysis of the (311) and (440) reflections yields the crystallite size $d_{XRD} \simeq 11(3)$ nm.

Elemental analysis of the sample Fe_3O_4@HCS shows a weight percentage of carbon of about 53.7(5) w%, as well as residuals of nitrogen of 2.7(5) w% and 1.5(5)w% of hydrogen. We hence conclude that the remaining mass fraction of 42.1w% amounts to the iron oxide content in the composite.

For the unambiguous determination of the iron oxide phase present, XPS measurements were performed which can differentiate the presence of Fe^{2+} and Fe^{3+} ions. Fig. 2 shows the XP spectra of Fe2*p* of Fe_3O_4@HCS and HCS. The spectra on Fe_3O_4@HCS display broad peaks at 710.6 ($2p_{3/2}$) and 724.2 eV ($2p_{1/2}$) which are typical of Fe_3O_4 [30]. In addition, Fe_2O_3 can be excluded since the characteristic satellite peak at 719.2 eV is not perceptible [33]. These findings clearly rule out the presence of Fe_2O_3 and imply that the formed oxide in the hybrid nanomaterial is Fe_3O_4. Note, that an additional peak at around 704 eV which is visible in both pure HCS and Fe_3O_4@HCS spectra is the characteristic In $3p_{1/2}$ line of the indium substrate used. Complementary XPS data can be found in the Supporting Information. In particular, the survey spectrum in S1a displays the presence of O, C, In and Fe without any detectable impurity. The comparison of C1s spectra of pure HCS and Fe_3O_4@HCS (S1b) as well as the respective Raman spectra (S2) show moreover no change of the carbon structure during the functionalization of HCS with the iron oxide nanoparticles, which demonstrates the HCS as a well-preserved, well-conducting carbon buffer matrix for the ultra-small magnetite nanoparticles.

The typical spherical shape of both as-synthesized HCS and Fe_3O_4@HCS is confirmed by SEM and TEM studies which visualize the morphology and micro-structure of the materials (see Fig. 3). In Fe_3O_4@HCS, in addition to bare HCS (Fig. 3a,b) which are about 150 nm in diameter, the images Fig. 3c to f show the presence of evenly dispersed nano-sized iron oxide particles. High-resolution TEM images (shown in Fig. 3f,h) additionally highlight that the iron oxide particles, are not loosely deposited on the HCS, they are embedded in the HCS framework. The observed crystalline region in Fig. 3h marked in red, displays a d-spacing of 0.25 nm an can hence be attributed to the (311)-plane of Fe_3O_4.

Additionally the TEM-EDX measurements (see Fig. S3 in the Supplement) furthermore prove the uniform distribution of Fe, O, and C. We note the exceptionally small size of the nanoparticles which display a maximum diameter well below 20 nm. This agrees to the results of the XRD analysis which implies crystallites with an average diameter of $d_{XRD} \simeq 11$ nm. One can hence conclude that most of the iron oxide particles are single crystalline.

3.2. Magnetic properties

The presence of ferromagnetism in Fe_3O_4 renders magnetic studies a meaningful tool to further investigate iron oxide nanoparticles in a hybrid nanomaterial [34]. While the weak diamagnetic contribution of carbon can be neglected, the magnetization curve in Fig. 4b confirms the overall ferromagnetic response of Fe_3O_4@HCS. Quantitatively, the observed saturation magnetization amounts to about 18 erg/$g_{Fe_3O_4}$ which is much lower than that of bulk Fe_3O_4 ($M_s = 92$ erg/$g_{Fe_3O_4}$) [35]. Reduced saturation magnetization of iron oxide nanoparticles is a known phenomenon and is attributed to surface effects, which, in nanoparticles, can dominate the properties due to the large surface to bulk ratio [30,36].

The difference in field-cooled (fc) and zero-field-cooled (zfc) magnetization data which is observed upon cooling below about 100 K confirms the presence of superparamagnetism in Fe_3O_4@HCS (Fig. 4b). This is also visible in the M vs. B curves in Fig. 4a which display a significant increase of the hysteresis, i.e., of the critical field, upon cooling to 2 K. The data allow to read-off the characteristic blocking temperature T_B which is particularly evident when the derivative of the difference of M_{fc} and M_{zfc} is considered (see the inset in Fig. 4b) [37, 38]. The peak in $\partial(M_{fc} - M_{zfc})/\partial T$ at $T_B \approx 5$ K implies the characteristic blocking temperature. Note, that the observation of a small hysteresis above T_B suggests that few particles remain blocked up to about 100 K, which is also the maximum of the zfc curve and therefore implies another characteristic blocking temperature. As the blocking temperature depends on the particle size, this suggests a certain distribution of particle sizes with however a clear signature attributed to the mean. From T_B, the mean particle volume can be estimated as [39]

$$V = \frac{T_B 25 k_B}{K_u} \tag{2}$$

with k_B the Boltzman constant and K_u the magnetic anisotropy constant. Using the anisotropy constant of bulk Fe_3O_4 of 1.35×10^4 Jm^{-3} [40]

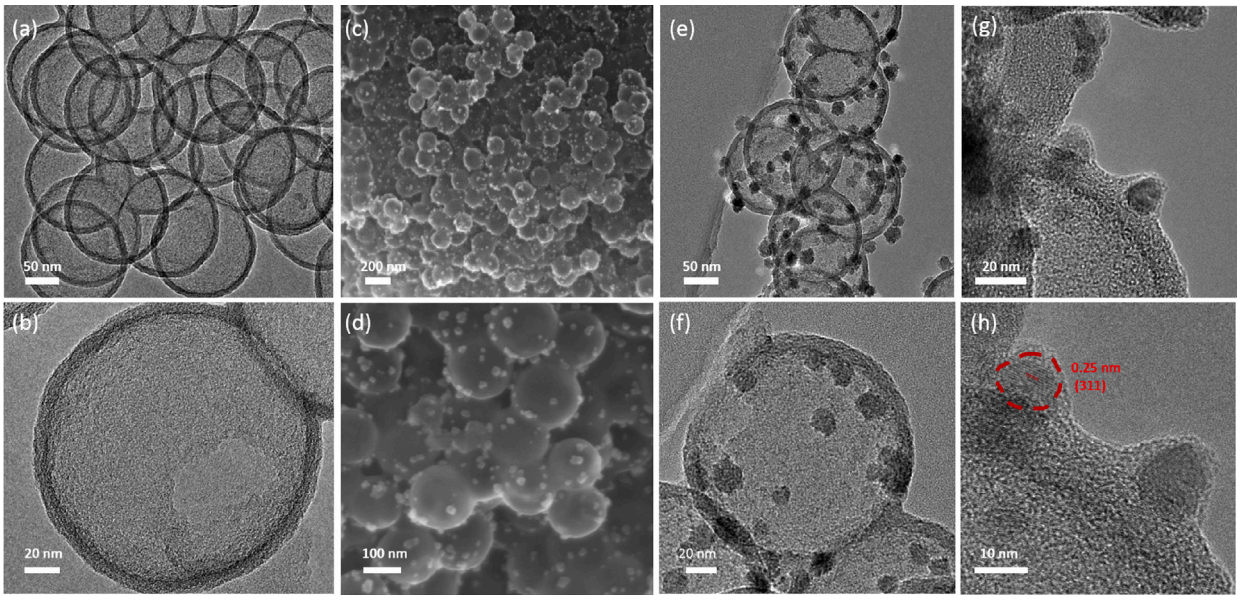

Fig. 3. TEM images of HCS (a,b) as well as SEM (c,d) and TEM (e-h) images of Fe_3O_4@HCS. The red color used marks a crystalline region.

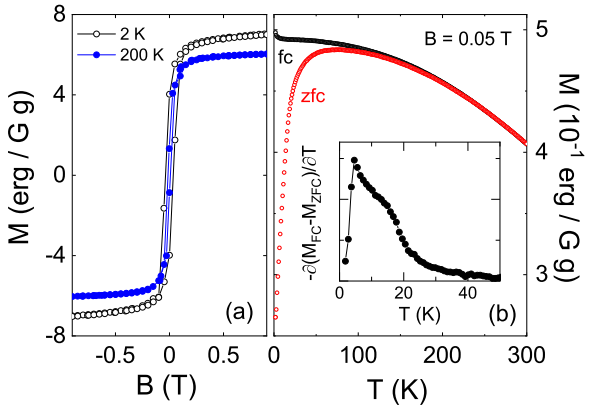

Fig. 4. (a) Magnetization of Fe_3O_4@HCS vs. magnetic field, at 2 K and 200 K and (b) vs. temperature at $B = 0.05$ T. The inset shows the derivative of the difference between field-cooled (fc) and zero-field-cooled (zfc) magnetization.

and the two characteristic temperatures, the average particle diameter can be roughly estimated to ~10 nm which agrees to the analysis of the TEM data and d_{XRD}. The sharp low-temperature peak at 5 K in particular indicates particles of 6 nm in diameter in the material.

3.3. Electrochemical studies

The hierarchical structure of Fe_3O_4@HCS featuring nano-sized particles of the oxide conversion material embedded in a hollow carbon matrix was studied by cyclic voltammetry and galvanostatic cycling (GCPL) in the voltage range of 0.01 – 3 V vs. Li/Li^+. In order to assess the effects of the carbon matrix, measurements were performed on pristine HCS under the same conditions. The complete electrochemical reaction path of bulk Fe_3O_4 can be expressed as follows [10,17,41]:

$$Fe_3O_4 + 2Li^+ + 2e^- \rightarrow Li_2Fe_3O_4 \quad (3)$$

$$Li_2Fe_3O_4 + 2e^- + 2Li^+ \leftrightarrow 2(Li_2O \cdot FeO) + Fe \quad (4)$$

$$FeO + 2e^- + 2Li^+ \leftrightarrow Fe + Li_2O \quad (5)$$

$$Fe_3O_4 + 8Li^+ + 8e^- \rightarrow 3Fe + 4Li_2O \quad (6)$$

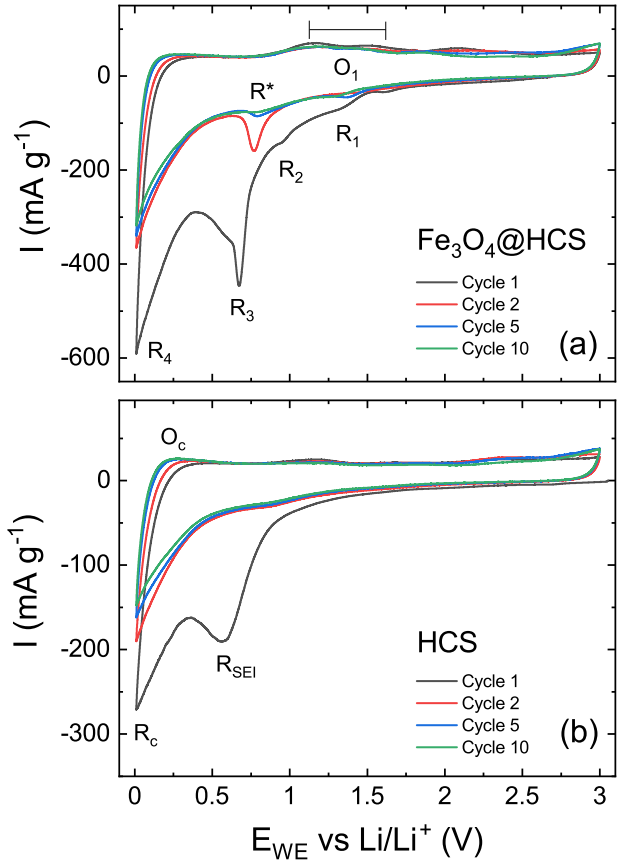

Fig. 5. Cyclic voltammogramms of cycle 1, 2, 5, and 10 of (a) Fe_3O_4@HCS and (b) HCS measured at a scan rate of 0.1 mV s^{-1}. The labels *R/O* mark distinct reduction and oxidation features.

Various processes can be identified in the cyclic voltammogramms (CVs) presented in Fig. 5. For pristine HCS (see Fig. 5b) the data indicate the formation of a passivating SEI (solid electrolyte interface) on the carbon surfaces as evidenced by the first-cycle reduction peak

(R_{SEI}) at 0.6 V [42]. Correspondingly, the SEI peak disappears upon further cycling. In addition, the data show a reduction/oxidation pair at 0.01/0.2 V (R_C/O_C) attributed to the reversible de-/lithiation into the carbon structures. Both the evolution of the features upon cycling, as well as tiny peaks around 0.8 V (reduction) and 1.2 V (oxidation), originating from lithium insertion/extraction into/from defects in the carbon structure, are typical for pristine HCS [43–47]. For Fe_3O_4@HCS, there are several additional features indicating the electrochemical activity of iron oxide (Fig. 5a). The first cycle is fundamentally different from the following ones and displays the irreversible transformation of Fe_3O_4 during the first lithiation in agreement with previous reports [9,10,41,48,49]. The first peak at 1.4 V is assigned to the initial incorporation of Li^+ cations into the Fe_3O_4 structure (Eq. (3)), the second peak at 1.0 V corresponds to the phase change from spinel Fe_3O_4 to rock salt FeO during additional Li^+ incorporation (Eq. (4)), and the third peak at 0.6 V is assigned to both the conversion reaction FeO to elemental Fe (Eq. (5)) and the formation of the SEI. Upon subsequent delithiation, Fe_3O_4 does not reappear but the FeO structure is formed in the O1 region [1,9,10]. In the subsequent cycles the reversible $Fe^{2+} \leftrightarrow Fe^0$ reaction is the remaining reaction happening in the R*/O1 region, leading to a theoretical reversible bulk capacity of Fe_3O_4 after the first cycle of 694 $mAhg^{-1}$ [10].

The galvanostatic cycling performance of Fe_3O_4@HCS with respect to pristine HCS-based electrodes is shown in Fig. 6a where dis-/charge capacities are presented. Fe_3O_4@HCS shows an initial discharge capacity of 1620 mAh g^{-1}. In contrast, the first charge yields only 600 mAh g^{-1}. The reason for the significantly higher discharge capacity can be traced back to firstly, the irreversible formation of the SEI and secondly, the irreversible conversion of Fe_3O_4, both taking place in the voltage region below 1 V (see the potential profile of the first cycle in Fig. 6b), which results in an irreversible capacity component of the first discharge cycle. In the next 20 cycles, a further slight decrease in the converted specific capacity towards 520 mAh g^{-1} is observed. Thereafter, the converted capacity increases steadily up to 1050 mAh g^{-1} in cycle 240 and then levels off slightly. Note, that the measured specific capacity of Fe_3O_4@HCS-based electrodes after 250 cycles significantly exceeds the postulated theoretical reversible capacity even for pure iron oxide of 694 mAh g^{-1}. As it will be discussed below, the exceedingly small size of the initial Fe_3O_4 nanoparticles presented here may be advantageous for the effect of additional capacity [10]. It is noteworthy that over the entire number of cycles, discharging converts more capacity than charging. The same trend is reflected in the Coulombic efficiency (see Fig. S4a), which displays an increase over the entire 250 cycles. The sharp increase in the first cycles is due to the step wise decrease of the irreversible components of the first discharge cycles. In the almost constant capacity range up to cycle 50, the coulombic efficiency increases to 96%, which is also clearly visible in the reduced gap between discharge capacity and charge capacity. In the next 200 cycles, the increase becomes smaller and smaller until finally a coulombic efficiency of 98.5% is reached in cycle 250. Meanwhile, pure HCS shows initial irreversibility and rather constant capacity upon cycling similar to previous reports [50,51]. An estimate of the contribution of only the Fe_3O_4 component in Fe_3O_4@HCS to the converted specific capacity can be made by subtracting the capacity of HCS according to its mass fraction. The resulting capacity of the ultrasmall Fe_3O_4-nanoparticles in the hybrid materials is shown in Fig. 6a. After a few cycles, it displays a reversible capacity of about 820 mAh $g^{-1}_{Fe_3O_4}$. As already qualitatively seen by the rather constant cycling performance of pure HCS, the increase in capacity of Fe_3O_4@HCS is due to the Fe_3O_4-subsystem which reaches more than 2000 mAh $g^{-1}_{Fe_3O_4}$ after 250 cycles. This value by far exceeds the theoretical reversible capacity associated with the electrochemical reactions shown above, clearly insinuating an enormous additional mechanism of charge storage.

Further insight into this phenomenon is gained by considering the corresponding potential curves in cycles 50, 100 and 200 shown in Fig. 6b. The potential curves of the discharge cycles imply due to the large overlap of the curves at high voltages that the increase in the achieved specific capacity upon cycling is mostly achieved in the low voltage range below 1 V. Since a low average discharge potential is considered as the main criterion for the positive prospect of industrial

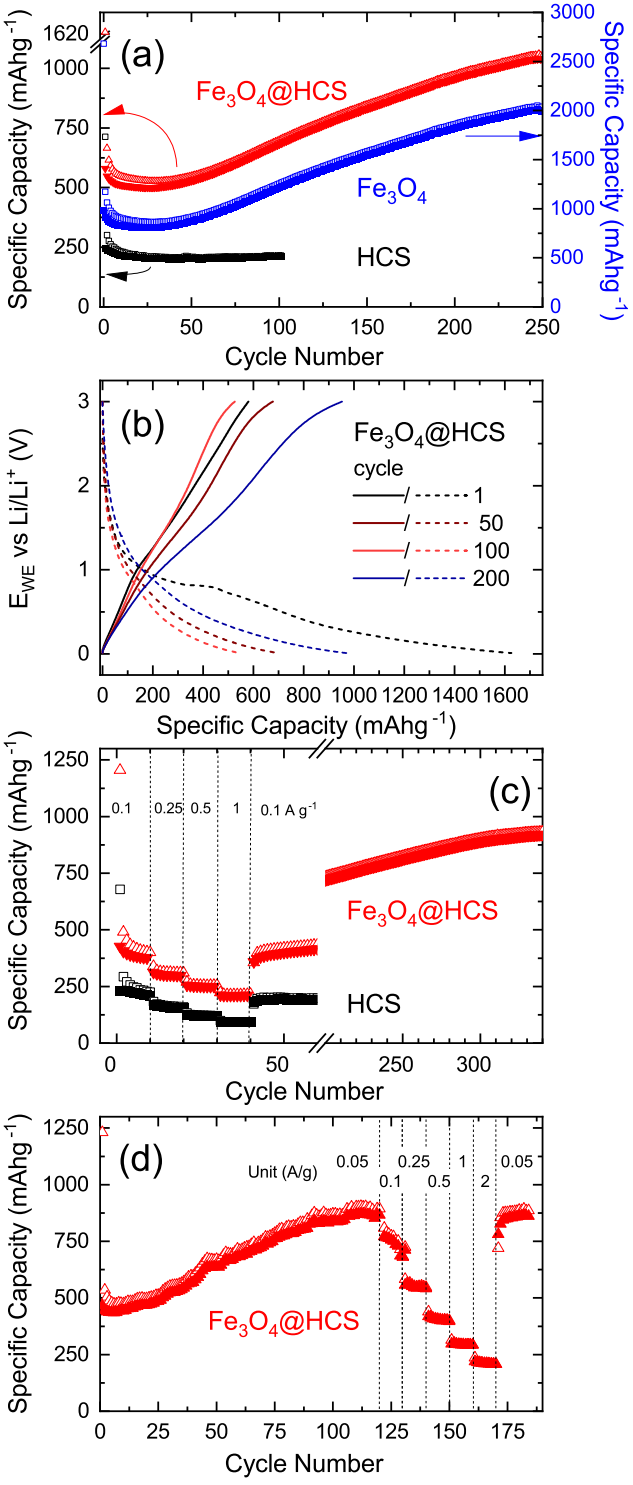

Fig. 6. (a) Specific charge/discharge capacities of Fe_3O_4@HCS and HCS electrodes at 100 mA g^{-1} between 0.01 and 3 V. (b) Selected corresponding potential profiles of Fe_3O_4@HCS electrodes. (c) Rate capacities with different cycling rates of Fe_3O_4@HCS and HCS electrode. (d) Rate capacities obtained at different cycling rates of Fe_3O_4@HCS after 120 cycles at 0.05 Ag^{-1}. Full/open markers indicate de/lithiation.

application, the result that the pronounced additional storage process occurs at low voltages is of utmost importance [52]. The low average discharge potential of our Fe_3O_4@HCS of about 0.5 V makes it again stand out compared to other Fe_3O_4 composites whose average discharge potential is around 1 V [9,53–56] and demonstrates its outstanding properties also from this point of view. From the charge curves it becomes apparent that strong differences upon charging in different cycles appear only in the range of more than one volt. These findings indicate a large voltage hysteresis of the underlying process, which is a common phenomenon in conversion based materials [57].

In Fig. 6c the superior performance of Fe_3O_4@HCS is shown by the rate capability test. It yields a reversible capacity of 400, 310, 250 and 200 mAh g^{-1}, respectively, for Fe_3O_4@HCS and 230, 170, 130, 100 mAh g^{-1} for HCS at currents of 0.1, 0.25, 0.5, 1 A g^{-1}. When the current density is set again to 0.1 A g^{-1}, the reversible capacity reaches 400 mAh g^{-1} demonstrating excellent reversibility of the Fe_3O_4@HCS-based electrode. Notably, as cycling continues, the capacity begins to immediately increases. Just shortly before the 300th cycle, the capacity hardly increases further and remains constant at a value of around 1000 mAh g^{-1} for the next 40 cycles.

To investigate the rate capability of Fe_3O_4@HCS in the regime where the capacity has increased upon cycling, a rate capability study was performed after 120 cycles at 0.05 Ag^{-1} when the reversible capacity reached 900 mAh g^{-1} (see Fig. 6d). The achieved capacity in the entire current range is about twice as high as compared to the rate measurements done in the beginning of cycling, so that at 0.1, 0.25, 0.5, 1 and 2 A g^{-1} a capacity of 750, 550, 400, 300 and 220 mAh g^{-1} is achieved, respectively. While the attained capacity increased significantly due to the decrease at higher current rates, the kinetic behavior remains similar to that observed in the initial cycles. Fig. S4a in the Supplement further shows that, at a consistently high current rate of 1 A g^{-1}, there is no large increase in capacity over 500 cycles. This indicates that the process which yields increasing capacity has slow kinetics or is unable to take place at high current rate. In contrast, in a constant current constant voltage (CCCV) measurement, the capacity gain per cycle significantly increases to around 20 mAh g^{-1} as shown in Fig. S4b. Note, that in this measurement the difference between charge and discharge is larger, too. In order to study whether and to which extent the capacity increases in the low voltage range alone, the voltage was limited from 0.01 to 1 V after the lithiation in cycle 13. The data in Fig. S4b after 13 cycles show that the capacity only increases minimally in the limited potential range from 0.01 to 1 V. The increase in capacity during cycling is therefore taking place over the entire voltage range.

Electrochemical impedance measurements on Fe_3O_4@HCS provide further insights into the electrochemical processes and their kinetics. The measurements have been performed at specific states of charge at frequencies between 200 kHz and 0.1 Hz (see Fig. S5). In Fig. 7 the corresponding Nyquist diagrams are displayed as well as fits to the data performed using the function Z Fit of the software EC-Lab (Bio-Logic) and the equivalent circuit shown in Fig. S6. The obtained fitting parameters are shown in Table S1.

After OCV, the Nyquist plot features a depressed semicircle in the high to medium frequency range reflecting the charge transfer (CT) resistance between electrolyte and electrode material. This is followed by a steep increase in the low-frequency range which slope represents the Li^+ diffusion impedance. The EIS after the first discharge displays an elevated high-frequency semicircle and in addition, a further, clearly visible semicircle starts to appear in the medium frequency range. Upon first charging, the 2nd semicircle disappears. The same trend, with an even more pronounced effect, is also detected after 10 cycles. Here again, it is evident that when fully charged, only a small semicircle is visible, whereas after complete discharge, two, now very pronounced semicircles are present. A quantitative analysis by fitting the data with the appropriate equivalent circuit (see Fig. S6) yields the enables to assess the effect of cycling on the electrolyte and CT resistances (R_E and R_{ct}), and double layer capacitance (Q_{ct}) (Table S1). The results

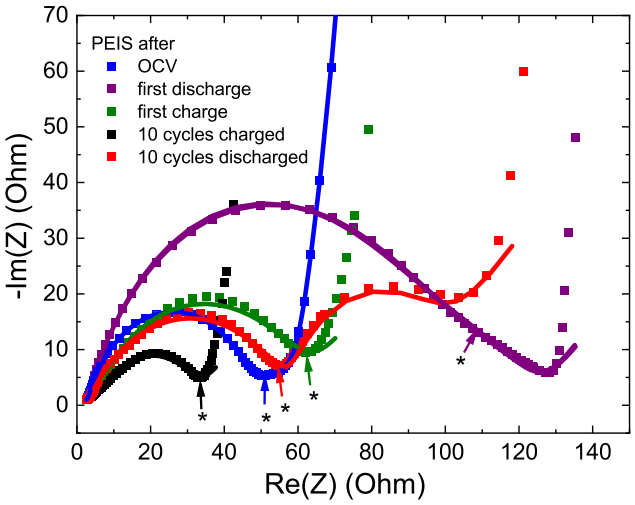

Fig. 7. Nyquist plot for Fe_3O_4@HCS measured at different state of charge. Solid lines show fits according to the equivalent circuit used (see the text). The arrows/asterisks mark the measured impedance at the frequency 10 Hz.

confirm and specify the qualitative conclusions. In particular, the data yield $R_E \sim 3\ \Omega$ while the CT resistance amounts to around ~50 Ω and Q_{ct} ~5 μF. R_{ct} as well as Q_{ct} are of the same magnitude as reported in Ref. [48]. A main observation in the EIS profiles is the appearance of the additional depressed semicircle in the discharged state which in the equivalent circuit is modeled by R_2 and Q_2. Such a feature is normally attributed to an additional capacitance surface layer. Our data imply that this surface layer is successively formed and disappearing as well as growing upon cycling. This scenario is corroborated by the fact that it is associated with a much slower process as can be nicely seen when considering the impedance response at a certain frequency, i.e., here 10 Hz, which is illustrated by the asterisks in Fig. 7. Specifically, the impedance response at 10 Hz always is in the minimum following the first semicircle. This observation allows two conclusions: (1) The newly appearing 2nd semicircle clearly is associated with a distinct and slower process with an innate time constant. (2) For all states under study, the high-frequency semicircle is characterized by a similar kinetics and can be assigned to the same layer. In addition, the observation that the 2nd semicircle becomes much more pronounced upon cycling indicates a possible explanation for the increase of converted specific capacity because the associated capacitance Q_2 increases from 0.4 mF in the first cycle to 12 mF in cycle ten. The slower time constant of the evolving 2nd semicircle may also be the reason behind the observed slow-down of the observed rate-dependence of extra capacity at higher current rates in the GCPL and GCPL rate measurements. As will be further discussed below and following the literature, the second semicircle can be either associated with reactions including the SEI [1,16] or with deposited spin-polarized electrons at the iron nanoparticles surfaces [17], or both. Our results render the usual SEI as the sole explanation for the respective process very unlikely. Firstly, the fact that the 2nd semicircle largely recedes upon charging would indicate nearly complete regression of the SEI which is not very plausible. SEI-related processes are usually in the high-frequency regime while the 2nd semicircle at hand appears at intermediate time scales. Exemplarily, graphite shows two semicircles in the fully charged state which do not regress and from which the distinct high frequency semicircle corresponds to the SEI [58]. In Fe_3O_4@HCS, the PEIS response of the SEI may be merged in the first semicircle but a distinct process cannot be extracted from the data which we attribute to similar kinetics of both processes. Though usual SEI formation can be ruled out, surface side reactions of the SEI and the formed iron metal nanoparticles which may result in the reversible

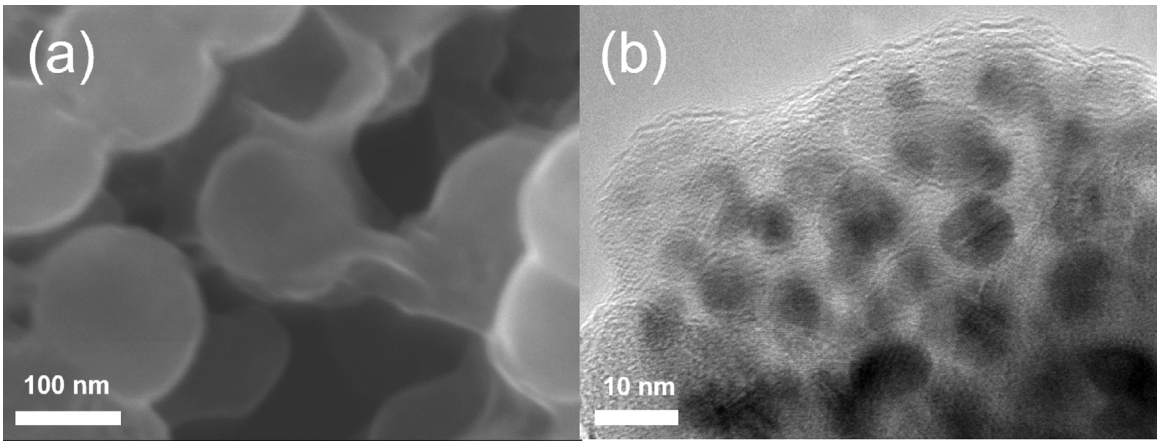

Fig. 8. (a) *Ex-situ* SEM and (b) *ex-situ* TEM images of a discharged Fe_3O_4@HCS-electrode.

Table 1
Electrochemical performance of various Fe_3O_4/carbon nanocomposites in LIBs.

Active material	Current (A g^{-1})	Cycle number	Capacity (mAh g^{-1})	Ref.
Fe_3O_4 nanoflakes-RGO	0.1	150	900	[60]
Yolk-double shell Fe_3O_4@C@C	0.5	250	800	[61]
Fe_3O_4@-tubular mesoporous carbon	0.2	60	850	[56]
Fe_3O_4@-N-doped porous carbon nanospheres	0.1	100	1240	[15]
Hierarchical 3D Fe_3O_4@porous carbon matrix	0.2 C	100	1077	[54]
Fe_3O_4 hollow nanospheres in honeycomb macroporous carbon	0.2	150	1050	[62]
Fe_3O_4@graphene quantum dots	0.1	200	900	[63]
Cake-like porous Fe_3O_4/C	0.1	100	600	[64]
Ultra-small Fe_3O_4@hollow carbon spheres	0.1	250	1050	This work

growth of a polymeric gel-like film are a possible explanation of the observed second semicircle [59].

A scenario involving interfacial storage theory suggests charge storage at the surface/contact area between the ionically conducting Li_2O-matrix (Li^+ storage) and the electrically conducting iron centers (e^- storage). In this scenario, an additional semicircle appearing in the mid frequency range of the EIS spectrum is proposed to signal such a capacitative storage mechanism [65,66]. Qualitatively, our observation of the mid-frequency extra semicircle only after charging seem to support this assignment. However, a rough estimate of the associated capacity based on geometrical considerations [67] questions this hypothesis, too (for details see the Supplemental Information, section Sd). Our measurements show that the reversibly accessible specific capacity associated with Fe_3O_4-nanoparticles in our material is about 1300 mAh g^{-1} larger than the postulated bulk capacity of Fe_3O_4. Since our data show that the formed iron nanoparticles are at least $d \sim 6$ nm in diameter, in a surface charge model the measured extra capacity would be associated with a surface capacitance of more than 10 mF cm^{-2}. This value is orders of magnitude larger than the maximum double layer capacitance of pure iron which is about 100 μF cm^{-2} [65,68]. We hence exclude a significant impact of the interfacial storage mechanism and, therefore, as an explanation for the observed strongly enhanced capacity [65,69]. We hence must conclude that surface side reactions of the formed iron metal nanoparticles and the SEI are most likely the dominant effect behind the high extra capacity as well as the observed additional medium frequency semicircle.

The effect of cycling on the materials microstructure is illustrated by Fig. 8 and Fig. S7 which displays *ex-situ* SEM and TEM images of Fe_3O_4@HCS-based electrodes after complete discharge. The SEM images (see Figs. 8a and Fig. S7a-d) show that the HCS substructure is practically unchanged even after 70 cycles, which confirms that the HCS matrix forms a very stable framework. The iron oxide nanoparticles on the contrary are no longer recognizable in the SEM image (Fig. 8a). We conclude that the formed iron nanoparticles are too small to be resolved by SEM. Instead, a new layer is observed which may be SEI and/or Li_2O [54] that spans over the HCS and even connects them (see Fig. S7c,d). This is also visible in corresponding TEM images in Fig. 8b and Fig. S7e,f which illustrate the material at complete discharge and a converted capacity of 800 mAh g^{-1}. Here, the formed iron particles are visible (black dots) and their size can be estimated to well below 10 nm. It is again noticeable that the iron particles are covered by some kind of layer, i.e., SEI or Li_2O, as was already seen by SEM. The layer even connects distant HCS with each other (see Fig. S7e).

To relate the electrochemical performance of Fe_3O_4@HCS presented here with other state-of-the-art Fe_3O_4 carbon composites from the literature, Table 1 shows the electrochemical properties of different Fe_3O_4 carbon composites. The table shows compatible or superior electrochemical performance of the Fe_3O_4@HCS composite as compared to other state-of-the-art Fe_3O_4 carbon composites.

4. Conclusions

In summary, a Fe_3O_4@HCS carbon composite is achieved by straightforward low-temperature synthesis, which avoids Oswald ripening of the ultra-small Fe_3O_4-particles (~10 nm) and furthermore yields a uniform dispersion of the nanoparticles on the stable HCS structure. The resulting hierarchical structure not only effectively prevents the disadvantages of Fe_3O_4 such as pulverization due to the large volume expansion upon electrochemical cycling, but moreover provides access to extra capacity resulting from the nano-nature of Fe_3O_4. As a result, the designed Fe_3O_4@HCS exhibits a high specific capacity of 1050 mAh g^{-1} at 0.1 C and a stable cycling performance well above 300 cycles. Furthermore demonstrates our detailed electrochemical analysis combined with ex situ imaging that the process of the extra capacity and its increase originates from a gradual formation and disappearance of

a capacitive surface layer, hinting to reversible reactions between the formed iron metal particles and the SEI. Notably, the design strategy and the synthesis route have great potential to be extended to construct other remarkable transition metal based carbon composites.

CRediT authorship contribution statement

Lennart Singer: Conceptualization, Methodology, Investigation, Writing – original draft, Review & editing. **Wojciech Kukułka:** Synthesis, Investigation, Review & editing. **Elisa Thauer:** Investigation, Validation, Review & editing. **Nico Gräßler:** Validation, Review & editing. **Andika Asyuda:** Investigation. **Michael Zharnikov:** Investigation, Review & editing. **Ewa Mijowska:** Conceptualization, Synthesis, Review & editing, Supervision. **Rüdiger Klingeler:** Conceptualization, Methodology, Review & editing, Supervision.

Declaration of competing interest

Authors have no conflicts of interest to disclose.

Data availability

Data will be made available on request.

Acknowledgments

We are grateful for access to the instrument and technical support for SEM studies provided by J. Zaumseil's group at Heidelberg University. Support by Deutsche Forschungsgemeinschaft (DFG) through project KL 1824/12-1, by BMBF via the project SpinFun (13XP5088) and within the framework of the Excellence Strategy of the Federal and State Governments of Germany is acknowledged. We are also grateful for support via project UMO-2016/23/G/ST5/04200 (Beethoven 2) by the National Science Centre Poland. A.A. acknowledges financial support by the DAAD-ACEH Scholarship of Excellence.

Appendix A. Supplementary data

Supplementary material related to this article can be found online at https://doi.org/10.1016/j.electacta.2023.142155.

References

[1] M.M. Thackeray, W. David, J.B. Goodenough, Structural characterization of the lithiated iron oxides $Li_xFe_3O_4$ and $Li_xFe_2O_3$ (0<x<2), Mater. Res. Bull. 17 (6) (1982) 785–793.
[2] P. Poizot, S. Laruelle, S. Grugeon, L. Dupont, J.M. Tarascon, Nano-sized transition-metal oxides as negative-electrode materials for lithium-ion batteries, Nature 407 (6803) (2000) 496–499.
[3] S. Gu, A. Zhu, Graphene nanosheets loaded Fe_3O_4 nanoparticles as a promising anode material for lithium ion batteries, J. Alloys Compd. 813 (2020) 152160.
[4] X. Yan, H. Ge, Y. Fang, Q. Liu, J. Gu, In situ ion–exchange synthesis of Fe_3O_4 nanosheets with 3D hierarchically porous carbon frameworks for high–performance energy storage, Energy Technol. 10 (7) (2022) 2200207.
[5] J. Cabana, L. Monconduit, D. Larcher, M.R. Palacín, Beyond intercalation-based Li-ion batteries: The state of the art and challenges of electrode materials reacting through conversion reactions, Adv. Mater. 22 (35) (2010) E170–92.
[6] D. Vernardou, M. Apostolopoulou, N. Katsarakis, E. Koudoumas, C. Drosos, I.P. Parkin, Electrochemical properties of APCVD α-Fe_2O_3 nanoparticles at 300 °C, ChemistrySelect 1 (10) (2016) 2228–2234.
[7] D. Vernardou, A. Kazas, M. Apostolopoulou, N. Katsarakis, E. Koudoumas, Cationic effect on the electrochemical characteristics of the hydrothermally grown manganese dioxide, J. Electron. Mater. 46 (4) (2017) 2232–2240.
[8] M. Valvo, C. Floraki, E. Paillard, K. Edström, D. Vernardou, Perspectives on iron oxide-based materials with carbon as anodes for Li- and K-ion batteries, Nanomaterials 12 (9) (2022) 1436.
[9] L. Li, H. Wang, Z. Xie, C. An, G. Jiang, Y. Wang, 3D graphene-encapsulated nearly monodisperse Fe_3O_4 nanoparticles as high-performance lithium-ion battery anodes, J. Alloys Compd. 815 (2020) 152337.
[10] D.C. Bock, A.C. Marschilok, K.J. Takeuchi, E.S. Takeuchi, Deliberate modification of the solid electrolyte interphase (SEI) during lithiation of magnetite, Fe_3O_4: Impact on electrochemistry, Chem. Commun. 53 (98) (2017) 13145–13148.
[11] J. Wang, Q. Hu, W. Hu, W. Zhu, Y. Wei, K. Pan, M. Zheng, H. Pang, Preparation of hollow core-shell Fe_3O_4/nitrogen-doped carbon nanocomposites for lithium-ion batteries, Molecules 27 (2) (2022) 396.
[12] M.D. Bhatt, J.Y. Lee, High capacity conversion anodes in Li-ion batteries: A review, Int. J. Hydrogen Energy 44 (21) (2019) 10852–10905.
[13] Y. Lu, L. Yu, X.W. Lou, Nanostructured conversion-type anode materials for advanced lithium-ion batteries, Chem 4 (5) (2018) 972–996.
[14] L. Fu, C.-C. Chen, J. Maier, Interfacial mass storage in nanocomposites, Solid State Ionics 318 (2018) 54–59.
[15] J. Mao, D. Niu, N. Zheng, G. Jiang, W. Zhao, J. Shi, Y. Li, Fe_3O_4-embedded and N-doped hierarchically porous carbon nanospheres as high-performance lithium ion battery anodes, ACS Sustain. Chem. Eng. 7 (3) (2019) 3424–3433.
[16] Y.-Y. Hu, Z. Liu, K.-W. Nam, O.J. Borkiewicz, J. Cheng, X. Hua, M.T. Dunstan, X. Yu, K.M. Wiaderek, L.-S. Du, K.W. Chapman, P.J. Chupas, X.-Q. Yang, C.P. Grey, Origin of additional capacities in metal oxide lithium-ion battery electrodes, Nat. Mater. 12 (12) (2013) 1130–1136.
[17] Q. Li, H. Li, Q. Xia, Z. Hu, Y. Zhu, S. Yan, C. Ge, Q. Zhang, X. Wang, X. Shang, S. Fan, Y. Long, L. Gu, G.-X. Miao, G. Yu, J.S. Moodera, Extra storage capacity in transition metal oxide lithium-ion batteries revealed by in situ magnetometry, Nat. Mater. 20 (1) (2021) 76–83.
[18] J. Jamnik, J. Maier, Nanocrystallinity effects in lithium battery materials, Phys. Chem. Chem. Phys. 5 (23) (2003) 5215.
[19] J. Maier, Mass storage in space charge regions of nano-sized systems (nano-ionics. Part V), Faraday Discuss. 134 (2007) 51–66, discussion 103–18, 415–9.
[20] Y.F. Zhukovskii, P. Balaya, E.A. Kotomin, J. Maier, Evidence for interfacial-storage anomaly in nanocomposites for lithium batteries from first-principles simulations, Phys. Rev. Lett. 96 (5) (2006) 058302.
[21] S. Klink, E. Madej, E. Ventosa, A. Lindner, W. Schuhmann, F. La Mantia, The importance of cell geometry for electrochemical impedance spectroscopy in three-electrode lithium ion battery test cells, Electrochem. Commun. 22 (2012) 120–123.
[22] M. Ender, J. Illig, E. Ivers-Tiffée, Three-electrode setups for lithium-ion batteries, J. Electrochem. Soc. 164 (2) (2017) A71–A79.
[23] H. Nara, D. Mukoyama, R. Shimizu, T. Momma, T. Osaka, Systematic analysis of interfacial resistance between the cathode layer and the current collector in lithium-ion batteries by electrochemical impedance spectroscopy, J. Power Sources 409 (2019) 139–147.
[24] M. Gaberšček, Understanding Li-based battery materials via electrochemical impedance spectroscopy, Nat. Commun. 12 (1) (2021) 6513.
[25] Y. Zubavichus, A. Shaporenko, M. Grunze, M. Zharnikov, Innershell absorption spectroscopy of amino acids at all relevant absorption edges, J. Phys. Chem. A 109 (32) (2005) 6998–7000.
[26] G.S. Zakharova, L. Singer, Z.A. Fattakhova, S. Wegener, E. Thauer, Q. Zhu, E.V. Shalaeva, R. Klingeler, MoO_2/C composites prepared by tartaric acid and glucose-assisted sol-gel processes as anode materials for lithium-ion batteries, J. Alloys Compd. 863 (2021) 158353.
[27] C. Pecharromn, T. Gonzlez-Carreo, J. Iglesias, The infrared dielectric properties of maghemite, γ-Fe_2O_3, from reflectance measurement on pressed powders, Phys. Chem. Minerals 22 (1) (1995) 21–29.
[28] H.C. St. O'Neill, W.A. Dollase, Crystal structures and cation distributions in simple spinels from powder XRD structural refinements: $MgCr_2O_4$, $ZnCr_2O_4$, Fe_3O_4 and the temperature dependence of the cation distribution in $ZnAl_2O_4$, Phys. Chem. Minerals 20 (8) (1994) 541–555.
[29] R. Chalasani, S. Vasudevan, Form, content, and magnetism in iron oxide nanocrystals, J. Phys. Chem. C 115 (37) (2011) 18088–18093.
[30] J. Su, M. Cao, L. Ren, C. Hu, Fe_3O_4-graphene nanocomposites with improved lithium storage and magnetism properties, J. Phys. Chem. C 115 (30) (2011) 14469–14477.
[31] G.S. Zakharova, E. Thauer, A.N. Enyashin, L.F. Deeg, Q. Zhu, R. Klingeler, V_2O_3/C composite fabricated by carboxylic acid-assisted sol–gel synthesis as anode material for lithium-ion batteries, J. Sol-Gel Sci. Technol. 12 (2021) 700.
[32] A.L. Patterson, The scherrer formula for X-Ray particle size determination, Phys. Rev. 56 (10) (1939) 978–982.
[33] T. Radu, C. Iacovita, D. Benea, R. Turcu, X-Ray photoelectron spectroscopic characterization of iron oxide nanoparticles, Appl. Surf. Sci. 405 (2017) 337–343.
[34] K. Lipert, M. Ritschel, A. Leonhardt, Y. Krupskaya, B. Büchner, R. Klingeler, Magnetic properties of carbon nanotubes with and without catalyst, J. Phys. Conf. Ser. 200 (7) (2010) 072061.
[35] J. Popplewell, L. Sakhnini, The dependence of the physical and magnetic properties of magnetic fluids on particle size, J. Magnet. Magn. Mater. 149 (1–2) (1995) 72–78.
[36] G.C. Papaefthymiou, Nanoparticle magnetism, Nano Today 4 (5) (2009) 438–447.
[37] H. Mamiya, M. Ohnuma, I. Nakatani, T. Furubayashim, Extraction of blocking temperature distribution from zero-field-cooled and field-cooled magnetization curves, IEEE Trans. Magn. 41 (10) (2005) 3394–3396.
[38] S. Dietrich, S. Chandra, C. Georgi, S. Thomas, D. Makarov, S. Schulze, M. Hietschold, M. Albrecht, D. Bahadur, H. Lang, Design, characterization and magnetic properties of Fe_3O_4-nanoparticle arrays coated with PEGylated-dendrimers, Mater. Chem. Phys. 132 (2–3) (2012) 292–299.

[39] C.P. Bean, J.D. Livingston, Superparamagnetism, J. Appl. Phys. 30 (4) (1959) S120–S129.

[40] D.J. Dunlop, O. Oezdemir, Rock Magnetism: Fundamentals and Frontiers, 1. paperback ed. with corr., 2. ed., reprinted., in: Cambridge studies in magnetism, vol. 3, Cambridge Univ. Press, Cambridge, 2013.

[41] W. Zhang, D.C. Bock, C.J. Pelliccione, Y. Li, L. Wu, Y. Zhu, A.C. Marschilok, E.S. Takeuchi, K.J. Takeuchi, F. Wang, Insights into ionic transport and structural changes in magnetite during multiple-electron transfer reactions, Adv. Energy Mater. 6 (10) (2016) 1502471.

[42] P. Novák, F. Joho, M. Lanz, B. Rykart, J.-C. Panitz, D. Alliata, R. Kötz, O. Haas, The complex electrochemistry of graphite electrodes in lithium-ion batteries, J. Power Sources 97–98 (2001) 39–46.

[43] K. Wenelska, A. Ottmann, P. Schneider, E. Thauer, R. Klingeler, E. Mijowska, Hollow carbon sphere/metal oxide nanocomposites anodes for lithium-ion batteries, Energy 103 (2016) 100–106.

[44] J. Eom, D. Kim, H. Kwon, Effects of ball-milling on lithium insertion into multi-walled carbon nanotubes synthesized by thermal chemical vapour deposition, J. Power Sources 157 (1) (2006) 507–514.

[45] Y. Zhang, Q. Ma, S. Wang, X. Liu, L. Li, Poly(vinyl alcohol)-assisted fabrication of hollow carbon spheres/reduced graphene oxide nanocomposites for high-performance lithium-ion battery anodes, ACS Nano 12 (5) (2018) 4824–4834.

[46] K. Tang, R.J. White, X. Mu, M.-M. Titirici, P.A. van Aken, J. Maier, Hollow carbon nanospheres with a high rate capability for lithium-based batteries, ChemSusChem 5 (2) (2012) 400–403.

[47] X. Yue, W. Sun, J. Zhang, F. Wang, Y. Yang, C. Lu, Z. Wang, D. Rooney, K. Sun, Macro-mesoporous hollow carbon spheres as anodes for lithium-ion batteries with high rate capability and excellent cycling performance, J. Power Sources 331 (2016) 10–15.

[48] Y. Liu, J. Chen, Z. Liu, H. Xu, Y. Zheng, J. Zhong, Q. Yang, H. Tian, Z. Shi, J. Yao, C. Xiong, Facile fabrication of Fe_3O_4 nanoparticle/carbon nanofiber aerogel from fe-ion cross-linked cellulose nanofibrils as anode for lithium-ion battery with superhigh capacity, J. Alloys Compd. 829 (6058) (2020) 154541.

[49] Q. Peng, C. Guo, S. Qi, W. Sun, L.-P. Lv, F.-H. Du, B. Wang, S. Chen, Y. Wang, Ultra-small Fe_3O_4 nanodots encapsulated in layered carbon nanosheets with fast kinetics for lithium/potassium-ion battery anodes, RSC Adv. 11 (3) (2021) 1261–1270.

[50] K. Wenelska, A. Ottmann, D. Moszyński, P. Schneider, R. Klingeler, E. Mijowska, Facile synthesis N-doped hollow carbon spheres from spherical solid silica, J. Colloid Interf. Sci. 511 (2018) 203–208.

[51] E. Thauer, X. Shi, S. Zhang, X. Chen, L. Deeg, R. Klingeler, K. Wenelska, E. Mijowska, Mn_3O_4 encapsulated in hollow carbon spheres coated by graphene layer for enhanced magnetization and lithium-ion batteries performance, Energy 217 (2021) 119399.

[52] H. Zhang, L. Wang, H. Li, X. He, Criterion for identifying anodes for practically accessible high-energy-density lithium-ion batteries, ACS Energy Lett. 6 (10) (2021) 3719–3724.

[53] W. Deng, S. Ci, H. Li, Z. Wen, One-step ultrasonic spray route for rapid preparation of hollow Fe_3O_4/C microspheres anode for lithium-ion batteries, Chem. Eng. J. 330 (2017) 995–1001.

[54] S. Hao, B. Zhang, Y. Wang, C. Li, J. Feng, S. Ball, M. Srinivasan, J. Wu, Y. Huang, Hierarchical three-dimensional Fe_3O_4@porous carbon matrix/graphene anodes for high performance lithium ion batteries, Electrochimica Acta 260 (2018) 965–973.

[55] Y. Zhao, J. Wang, C. Ma, L. Cao, Z. Shao, A self-adhesive graphene nano-scroll/nanosheet paper with confined $Fe_{1-x}S/Fe_3O_4$ hetero-nanoparticles for high-performance anode material of flexible Li-ion batteries, Chem. Eng. J. 370 (2019) 536–546.

[56] Z. Cao, X. Ma, Encapsulated Fe_3O_4 into tubular mesoporous carbon as a superior performance anode material for lithium-ion batteries, J. Alloys Compd. 815 (2020) 152542.

[57] L. Li, R. Jacobs, P. Gao, L. Gan, F. Wang, D. Morgan, S. Jin, Origins of large voltage hysteresis in high-energy-density metal fluoride lithium-ion battery conversion electrodes, J. Am. Chem. Soc. 138 (8) (2016) 2838–2848.

[58] P. Zhang, T. Yuan, Y. Pang, C. Peng, J. Yang, Z.-F. Ma, S. Zheng, Influence of current density on graphite anode failure in lithium-ion batteries, J. Electrochem. Soc. 166 (3) (2019) A5489–A5495.

[59] X. Li, L. Qiao, D. Li, X. Wang, W. Xie, D. He, Three-dimensional network structured α-Fe_2O_3 made from a stainless steel plate as a high-performance electrode for lithium ion batteries, J. Mater. Chem. A 1 (21) (2013) 6400.

[60] Y.-H. Shi, K. Wang, H.-H. Li, H.-F. Wang, X.-Y. Li, X.-L. Wu, J.-P. Zhang, H.-M. Xie, Z.-M. Su, J.-W. Wang, H.-Z. Sun, Fe_3O_4 nanoflakes-RGO composites: A high rate anode material for lithium-ion batteries, Appl. Surf. Sci. 511 (2020) 145465.

[61] X. Wang, J. Wang, Z. Chen, K. Yang, Z. Zhang, Z. Shi, T. Mei, J. Qian, J. Li, X. Wang, Yolk-double shell Fe_3O_4@C@C composite as high-performance anode materials for lithium-ion batteries, J. Alloys Compd. 822 (2020) 153656.

[62] L. Wang, H. Zheng, X. Jin, Y. Yuan, Fe_3O_4 hollow nanospheres grown in situ in three-dimensional honeycomb macroporous carbon boost long-life and high-rate lithium ion storage, J. Electron. Mater. 52 (1) (2023) 10–22.

[63] F. Shi, Q. Liu, Z. Jin, G. Huang, B. Xing, J. Jia, C. Zhang, A facile method to prepare Fe_3O_4@CTP QDs composite as advanced anode material for lithium ion batteries, J. Alloys Compd. 890 (2022) 161911.

[64] J. Huang, Q. Dai, C. Cui, H. Ren, X. Lu, Y. Hong, S. Woo Joo, Cake-like porous Fe_3O_4@C nanocomposite as high-performance anode for Li-ion battery, J. Electroanalyt. Chem. 918 (2022) 116508.

[65] F. Baumann, J. Fleig, H. Habermeier, J. Maier, Impedance spectroscopic study on well-defined $(La,Sr)(Co,Fe)O_{3-\delta}$ model electrodes, Solid State Ionics 177 (11–12) (2006) 1071–1081.

[66] J. Jamnik, J. Maier, Treatment of the impedance of mixed conductors equivalent circuit model and explicit approximate solutions, J. Electrochem. Soc. 146 (11) (1999) 4183–4188.

[67] A. Ponrouch, P.-L. Taberna, P. Simon, M.R. Palacín, On the origin of the extra capacity at low potential in materials for Li batteries reacting through conversion reaction, Electrochimica Acta 61 (2012) 13–18.

[68] O.E. Barcia, O.R. Mattos, Reaction model simulating the role of sulphate and chloride in anodic dissolution of iron, Electrochimica Acta 35 (10) (1990) 1601–1608.

[69] R. Usiskin, J. Maier, Interfacial effects in lithium and sodium batteries, Adv. Energy Mater. 11 (2) (2021) 2001455.